GEOPHYSICS, VOL. 67, NO. 5 (SEPTEMBER-OCTOBER 2002); P. 1382–1395, 16 FIGS.
10.1190/1.1512784

Case History

Joint inversion of PP and PS reflection data for VTI media: A North Sea case study

Vladimir Grechka*, Ilya Tsvankin‡, Andrey Bakulin**, Jan Ove Hansen§, and Claude Signer§§

ABSTRACT

Despite the significant advantages of combining PP and PS reflection data in anisotropic parameter estimation, application of this approach has been hindered by the inherent complexity of PS-wave moveout. To overcome this problem, V. Grechka and I. Tsvankin suggested a model-independent procedure to construct the traveltimes of pure SS-wave reflections from PP and PS data. Here, we apply their method and anisotropic multicomponent stacking-velocity tomography to a 2-D line acquired over the lower Tertiary Siri reservoir in the North Sea.

The computed traveltimes of SS reflections from several horizons are used to estimate the effective SS-wave normal-moveout (NMO) velocities, which are combined with the NMO velocities of PP-waves in the tomographic velocity analysis. Comparison of the vertical and NMO velocities of the PP- and SS-waves provides clear evidence of anisotropy in the section above the reservoir. The interval parameter estimation is performed under the assumption that the section is composed of transversely isotropic layers with a vertical symmetry axis (VTI media). Since the subsurface structure is close to horizontally layered, the reflection data cannot be uniquely inverted for the VTI parameters without additional information (e.g., the vertical velocities found from borehole data).

The parameter-estimation algorithm produces a family of equivalent VTI models that fit the PP and PS (or SS) traveltimes equally well. Although the range of variations in ϵ and δ for the equivalent models is rather wide, it does not include isotropic media ($\epsilon = \delta = 0$), which implies that accurate matching of both PP and PS data is impossible without accounting for anisotropy. To overcome the nonuniqueness in the inversion of reflection data and build a VTI depth model, we use P-wave check shots acquired in the only borehole drilled on the processed line. Throughout the section $\epsilon > \delta$, with the largest values of both anisotropic coefficients observed in the depth range 0.7–1.5 km where ϵ reaches almost 0.25. Time sections of the original PS data computed using the VTI model have a much higher quality than the conventional isotropic sections.

INTRODUCTION

Building anisotropic velocity models is a critically important element in the characterization and monitoring of many hydrocarbon reservoirs (e.g., Thomsen, 1999; Bakulin et al., 2000). To carry out anisotropic parameter estimation even in the simplest case of vertical transverse isotropy (VTI media), one typically

Manuscript received by the Editor May 22, 2001; revised manuscript received December 18, 2001.
*Formerly Center for Wave Phenomena, Department of Geophysics, Colorado School of Mines, Golden, Colorado 80401-1887; presently Shell International Exploration and Production Inc., Bellaire Technology Center, 3737 Bellaire Boulevard, Houston, Texas 77001-0481. E-mail: grechka@unix.shell.com.
‡Colorado School of Mines, Center for Wave Phenomena, Department of Geophysics, Golden, Colorado 80401-1887. E-mail: ilya@dix.mines.edu.
**Formerly Schlumberger Cambridge Research, High Cross, Madingley Road, Cambridge, CB3 0EL, England; presently Shell International Exploration and Production Inc., 3737 Bellaire Boulevard, Houston, Texas 77001-0481. E-mail: abakulin@yahoo.com.
§Formerly Schlumberger Stavanger Research, Post Office Box 8013, N-4068, Stavanger, Norway; presently Statoil, Molnholtet 42, 9414 Harstad, Norway.
§§Schlumberger Cambridge Research, High Cross, Madingley Road, Cambridge, CB3 0EL, England.

has to record multicomponent data and supplement PP-wave moveout with reflection traveltimes of converted PS-waves (e.g., Thomsen, 1999; Tsvankin and Grechka, 2000a, b). Processing and inversion of PS-waves, however, are complicated by such properties of mode conversions as reflection-point dispersal, polarity reversal, and moveout asymmetry with respect to zero offset. The last problem, called the "diodic velocity" by Thomsen (1999), is the most serious because it precludes application of the conventional hyperbolic moveout equation to converted waves.

As a result, velocity analysis of PS-waves is often performed on common-image-point (CIP) gathers, which requires prestack migration of at least part of the data after each velocity update. Another computationally less expensive method is the so-called map migration (e.g., Iversen and Gjøystdal, 1996; Iversen et al., 2000), in which kinematic ray tracing essentially replaces prestack migration. Taking anisotropy into account, however, may increase the cost of ray tracing by several orders of magnitude (e.g., Tsvankin, 2001), which hinders the application of map migration.

An alternative approach to velocity analysis of PS-waves was recently suggested by Grechka and Tsvankin (2002b), who showed that the traveltimes of PP- and PS-waves reflected from the same interface are sufficient for constructing the traveltimes of the pure SS-waves for this reflector. Their algorithm for computing SS traveltimes is exact and entirely data-driven, so exact knowledge of the subsurface velocity field is not required. The obtained SS moveout is symmetric with respect to zero offset and can be processed by velocity-analysis methods developed for pure (nonconverted) modes.

Joint inversion of PP and SS traveltimes can be efficiently performed using the so-called "stacking-velocity tomography," which operates with NMO (stacking) velocities for 2-D lines and NMO ellipses for wide-azimuth 3-D surveys (e.g., Grechka et al., 2000a, b). For anisotropic models composed of homogeneous layers or blocks separated by smooth interfaces, the NMO ellipse of any pure-mode reflection at a given common-midpoint (CMP) location can be computed by tracing only one (zero-offset) ray (Grechka et al., 2000a, b; Grechka and Tsvankin, 2002a). This makes tomographic iterative inversion computationally feasible even for complex anisotropic models. Grechka et al. (2000a, b) developed a P-wave stacking-velocity tomography technique for VTI media composed of homogeneous layers separated by plane or smooth curved interfaces. This algorithm was extended by Grechka, Pech, and Tsvankin (2002, a companion paper in this issue) to multicomponent (PP and SS) data in transversely isotropic (TI) media with arbitrary tilt of the symmetry axis.

The results discussed above can be used to devise a complete inversion/processing sequence for joint anisotropic velocity analysis of PP- and PS-waves. The processing flow includes the following main steps:

1) Prestack horizon-consistent picking of PP and PS traveltimes on 2-D lines or 3-D data volumes and identifying the events reflected from the same interface, as done in the map migration of Iversen et al. (2000).
2) Computation of the traveltimes of the pure SS reflections from the PP and PS data using the method of Grechka and Tsvankin (2002b).
3) Inversion of the NMO velocities (in two dimensions) or NMO ellipses (in three dimensions), zero-offset traveltimes, and reflection slopes of the PP- and SS-waves for the interval anisotropic parameters (Grechka, Pech, and Tsvankin, 2002).

Here, we apply the proposed methodology to estimation of the interval VTI parameters of the section above the lower Tertiary Siri reservoir in the North Sea. Even though the data set includes long-offset PP and PS traveltimes, the absence of structural features with dips of at least 15°–20° makes the inversion for the vertical velocities and Thomsen's (1986) anisotropic parameters ϵ and δ nonunique (Tsvankin and Grechka, 2000a; Grechka and Tsvankin, 2003a). We obtain a family of kinematically equivalent VTI solutions, and show that isotropic models cannot fit both PP and PS data. Then P-wave check shots are used to remove the ambiguity and estimate the depth-varying parameters ϵ and δ.

PP AND PS TRAVELTIME DATA

The Siri survey includes three four-component (4-C) seabed seismic lines and an 8.7 km × 17.6 km 3-D towed-streamer data set that crosses the Norwegian-Danish North Sea border. The scope of this study is limited to 2-D processing of a portion of one of the 4-C lines. The initial P-wave velocity model was built using the 3-D data and then supplemented with shear-wave information obtained from a seabed line (Iversen et al., 2000). A detailed description of acquisition, model-based (isotropic) processing and interpretation, and the subsurface geology is in Signer et al. (2000). The deepest interpreted horizon (top Balder) is right above the top of the thin (∼30 m) Siri reservoir (Figure 1), and the structure of the overburden is close to being horizontally layered.

Prestack PP and PS (PSV) reflection traveltimes for all interpreted horizons in Figure 1 were obtained using Schlumberger's semi-automatic picker. The traveltime picks were made on common-receiver gathers with the receiver increment $\Delta r = 200$ m; the source increment within each gather was $\Delta s = 25$ m. Figure 2 shows typical raw PP and PS traveltime picks, which have several distinct features important for our analysis.

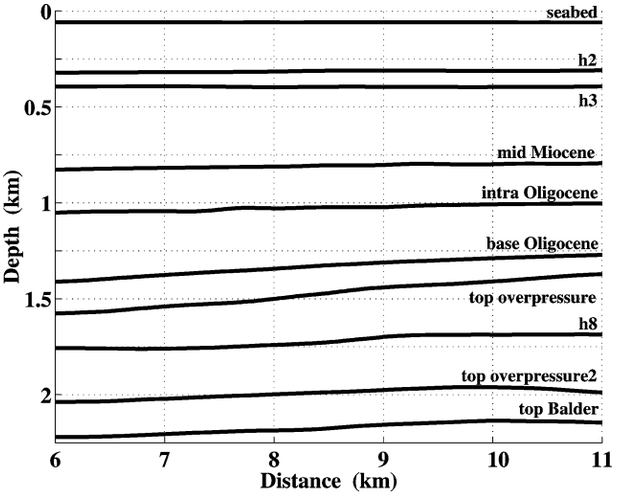

FIG. 1. Depth section above the Siri reservoir built by Signer et al. (2000).

1) The PP traveltime contours (Figure 2a) are almost symmetric with respect to zero offset. Their mild asymmetry can be largely attributed to the fact that the sources are located on the ocean surface, whereas the receivers are placed on the sea bottom. Another possible source of the traveltime asymmetry in Figure 2a is inaccurate traveltime picking. These errors will be estimated while performing velocity analysis.
2) The asymmetry of the PS traveltimes (see the discussion of "diodic velocity" in Thomsen, 1999) with respect to zero offset is much more pronounced (Figure 2b). The method of Grechka and Tsvankin (2002b), however, operates with local slopes on common-receiver gathers and does not rely on the symmetry of the moveout function. The most pronounced traveltime asymmetry of PS-waves is observed in the area of increased lateral variation in the traveltimes (indicative of lateral heterogeneity) near CMP location $x_{\mathrm{CMP}} = 8$ km (Figure 1).
3) The traveltimes in Figure 2 were picked for a wide range of offsets limited by $h_{\max,PP} \approx h_{\max,PS} \approx 4$ km, which yields the maximum offset-to-depth ratio for the top overpressure interface $h_{\max,PP}/z$ of approximately 2.5.

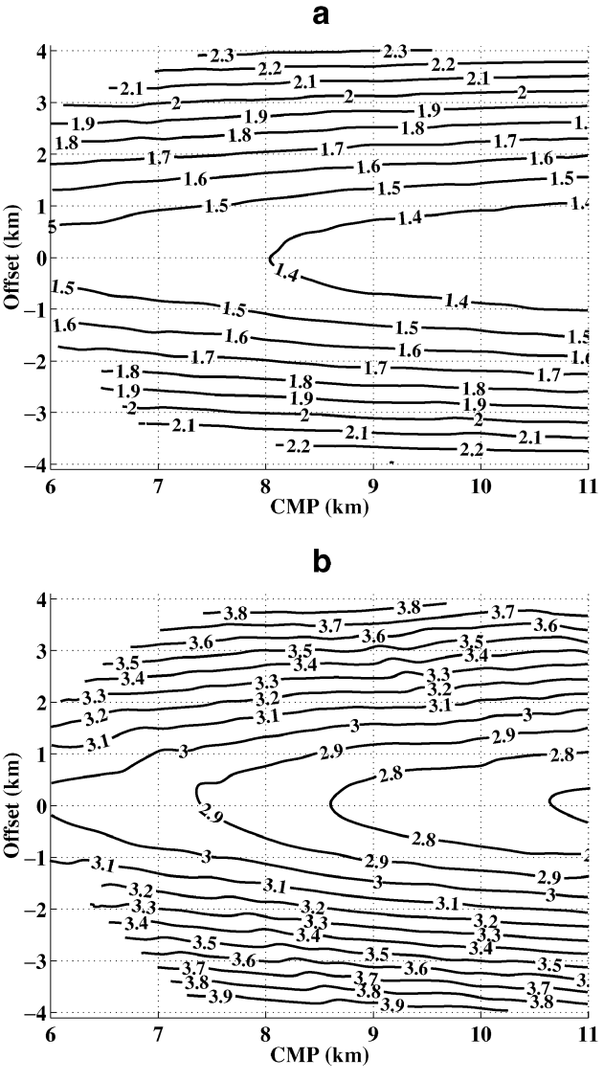

FIG. 2. Raw picked traveltimes (in seconds) of the PP (a) and PS (b) reflections from the top overpressure interface (see Figure 1) above the Siri reservoir. Offset $h(h = r - s)$ is either positive or negative depending on the sign of the difference between the receiver (r) and source (s) coordinates.

If the subsurface structure is nearly horizontally layered, as in the case of the Siri reservoir, the expected maximum offset $h_{\max,SS}$ of the constructed SS-traveltimes is approximately related to that of the PP-waves as (Tessmer and Behle, 1988; Grechka and Tsvankin, 2000b)

$$h_{\max,SS} \approx g\, h_{\max,PP}, \tag{1}$$

where g is the ratio of the S- and P-wave velocities,

$$g \equiv \frac{V_S}{V_P}. \tag{2}$$

Although equation (1) is derived for isotropic media, it can be used for qualitative analysis in moderately anisotropic VTI media if g is defined as the ratio of the vertical velocities V_{S0}/V_{P0}. For the overburden above the Siri reservoir, $g \approx 0.33$ (see below), which implies that for the top overpressure interface, $h_{\max,SS} \approx 1.3$ km and, therefore, $h_{\max,SS}/z \approx 0.82$. Thus, to obtain reliable estimates of SS-wave stacking velocities, it is necessary to acquire long-spread PP and PS moveout data. This conclusion is supported by the processing results below.

COMPUTATION OF REFLECTION TRAVELTIMES FOR THE SS-WAVES

In constructing the SS traveltimes from those of the PP and PS (PSV) reflections, we follow the general methodology of Grechka and Tsvankin (2002b). The processing of this particular data set, however, requires some adjustments because the sources and receivers are located at different depth levels (the sources are on the ocean surface, while the receivers on the ocean bottom). The processing flow used to obtain the shear-wave reflection traveltimes from each interface is as follows.

Step 1. Slowness estimation

The traveltimes $t_{PP}(s,r)$ and $t_{PS}(s,r)$ for a certain reflector are sorted into common-receiver gathers for a range of source coordinates s (r is the receiver coordinate). Differentiation of the traveltimes on common-receiver gathers with respect to the source coordinate results in the horizontal slowness components of the PP- and PS-waves [$p^s_{PP}(s,r)$ and $p^s_{PS}(s,r)$, "s" stands for source] at the source locations.

Step 2. Downward continuation

The source positions are mapped (projected) onto the ocean bottom along the rays specified by the horizontal slownesses $p^s_{PP}(s,r)$ and $p^s_{PS}(s,r)$. The vertical slowness components are computed as

$$q^s_{PP}(s,r) = \sqrt{\frac{1}{V_w^2} - \left[p^s_{PP}(s,r)\right]^2}$$

and

$$q^s_{PS}(s,r)=\sqrt{\frac{1}{V_w^2}-\left[p^s_{PS}(s,r)\right]^2},$$

where $V_w=1.5$ km/s is the velocity in the water. The vertical and horizontal slowness components fully specify the corresponding rays, which allows us to correct the traveltimes for the raypath in the water. The depth of the ocean bottom is taken to be equal to 60 m (Figure 1).

Step 3. Interpolation of source locations

We use interpolation to estimate the PP and PS traveltimes $t_{PP}(s,r)$, $t_{PS}(s,r)$ and their slownesses $p^s_{PP}(s,r)$, $p^s_{PS}(s,r)$ on a regular grid of source positions (some of which coincide with receiver positions) with fixed increment $\Delta s=25$ m.

Step 4. Building common-shot gathers

The traveltimes $t_{PP}(s,r)$ and $t_{PS}(s,r)$ are resorted into common-shot gathers. This is needed to facilitate the search (described in step 5) for the PP and PS arrivals with the same ray parameters at the source location.

Step 5. Matching reflection slopes

For each PP-wave source-receiver pair (s,r), we search for the PS-wave receiver coordinate ρ such that the PP-wave traveling from s to r and the PS-wave traveling from s to ρ have the same horizontal slowness (ray parameter) at the source s:

$$p^s_{PP}(s,r)=p^s_{PS}(s,\rho).$$

Steps 1–5 are designed to build a table (for all P-wave sources s and receivers r) containing the source and receiver coordinates of the PP and PS rays that are excited at the same location and have the same reflection point (Grechka and Tsvankin, 2002b).

Step 6. Computation of SS traveltimes

Consider two reciprocal PP rays, one of which is excited at s and recorded at r, while the other is excited at r and recorded at s (Figure 3). These rays have the same traveltime but, in general, the ray parameters at the source and receiver locations differ. Therefore, we can describe such reciprocal rays by the parameter vectors

$$\left[s,r,t_{PP}(s,r),\,p^s_{PP}(s,r)\right]\quad\text{and}\quad\left[r,s,t_{PP}(r,s),\,p^r_{PP}(r,s)\right].$$

Next, the table generated at the previous step is used to find two PS-rays, one excited at s and the other at r, that have the same reflection point R as does the PP reflection in Figure 3:

$$\left[s,\rho_1,t_{PS}(s,\rho_1),\,p^s_{PS}(s,\rho_1)\right]\quad\text{and}$$
$$\left[r,\rho_2,t_{PS}(r,\rho_2),\,p^r_{PS}(r,\rho_2)\right],$$

where

$$p^s_{PP}(s,r)=p^s_{PS}(s,\rho_1),$$
$$p^r_{PP}(r,s)=p^r_{PS}(r,\rho_2).$$

Note that the points with the coordinates s, r, ρ_1, and ρ_2 are located at the ocean bottom (step 2). Then, according to Grechka and Tsvankin (2002b), the traveltime of the SS reflection excited at ρ_1 and recorded at ρ_2 is given by

$$t_{SS}(\rho_1,\rho_2)=t_{PS}(s,\rho_1)+t_{PS}(r,\rho_2)-t_{PP}(s,r). \tag{3}$$

It is important to emphasize that the PP traveltimes in equation (3) are reciprocal with respect to the source and receiver positions,

$$t_{PP}(s,r)=t_{PP}(r,s), \tag{4}$$

which makes the SS traveltimes $t_{SS}(\rho_1,\rho_2)$ also reciprocal,

$$t_{SS}(\rho_1,\rho_2)=t_{SS}(\rho_2,\rho_1). \tag{5}$$

In contrast, the PS-wave traveltimes in equation (3) generally do not remain the same if the source and receiver positions are interchanged.

As an example, the computed SS-wave source and receiver coordinates ρ_1 and ρ_2 and the corresponding SS traveltimes $t_{SS}(\rho_1,\rho_2)$ for the top overpressure interface are shown in Figure 4. We observe the following features of the SS (SVSV) traveltime field:

1) Despite the mild asymmetry of the PP traveltimes in Figure 2a, both the SS-wave source and receiver positions and traveltimes in Figure 4 are symmetric with respect to zero offset. The symmetry of the SS data was enforced by replacing equation (3) with

$$t_{SS}(\rho_1,\rho_2)=t_{PS}(s,\rho_1)+t_{PS}(r,\rho_2)-\frac{1}{2}[t_{PP}(s,r)+t_{PP}(r,s)]. \tag{6}$$

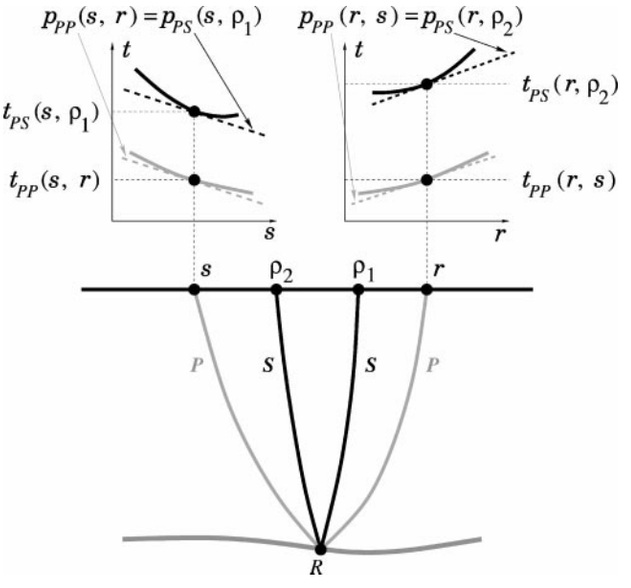

FIG. 3. Matching the pairs of reflection slopes $p^s_{PP}(s,r)$ and $p^s_{PS}(s,\rho_1)$, and $p^r_{PP}(r,s)$ and $p^r_{PS}(r,\rho_2)$ allows us to find the source-receiver coordinates ρ_1 and ρ_2 of the pure SS-ray with the trajectory $\rho_1 R\rho_2$. The constructed SS-ray has exactly the same reflection point R as the PP-ray sRr and the PS-rays $sR\rho_1$, $rR\rho_2$ (after Grechka and Tsvankin, 2002b).

This artificial adjustment should also help to suppress the noise that likely contributed to the asymmetry of the picked PP traveltimes.

2) The computed shear-wave offsets cluster in the range 0.4–1.2 km, with little coverage for larger offsets (Figure 4a). Hence, the maximum offset-to-depth ratio reaches 0.8 (see the previous section), which is marginally acceptable for SS-wave velocity analysis. The SS traveltimes for other horizons have similar offset-to-depth ratios (not shown here).

VELOCITY ANALYSIS OF PP AND SS DATA

The picked traveltimes of PP-waves (such as those in Figure 2a) and computed traveltimes of SS-waves (such as those in Figure 4b) can be used to estimate their associated zero-offset times (t_{P0} and t_{S0}) and stacking (moveout) velocities ($V_{\mathrm{nmo},P}$ and $V_{\mathrm{nmo},S}$). Since the sources and receivers for SS-waves are obtained on an irregular grid (see Figure 4a), there are several different ways of binning the SS data into CMP gathers. Since each gather averages information over a certain lateral distance, we elected to form composite gathers that include offset-traveltime pairs with the midpoints within a certain interval Δx_{CMP}. Clearly, increasing Δx_{CMP} should improve the stability of velocity estimates but reduce the number of gathers and the lateral velocity resolution along the line. By performing velocity analysis for a range of values of Δx_{CMP}, we found that $\Delta x_{\mathrm{CMP}} = 0.5$ km provides both sufficient stability and acceptable lateral resolution in estimating stacking velocities.

Figure 5 shows the obtained zero-offset traveltimes and stacking (NMO) velocities for the top of the Balder formation (i.e., the top of the Siri reservoir). Velocity analysis of SS

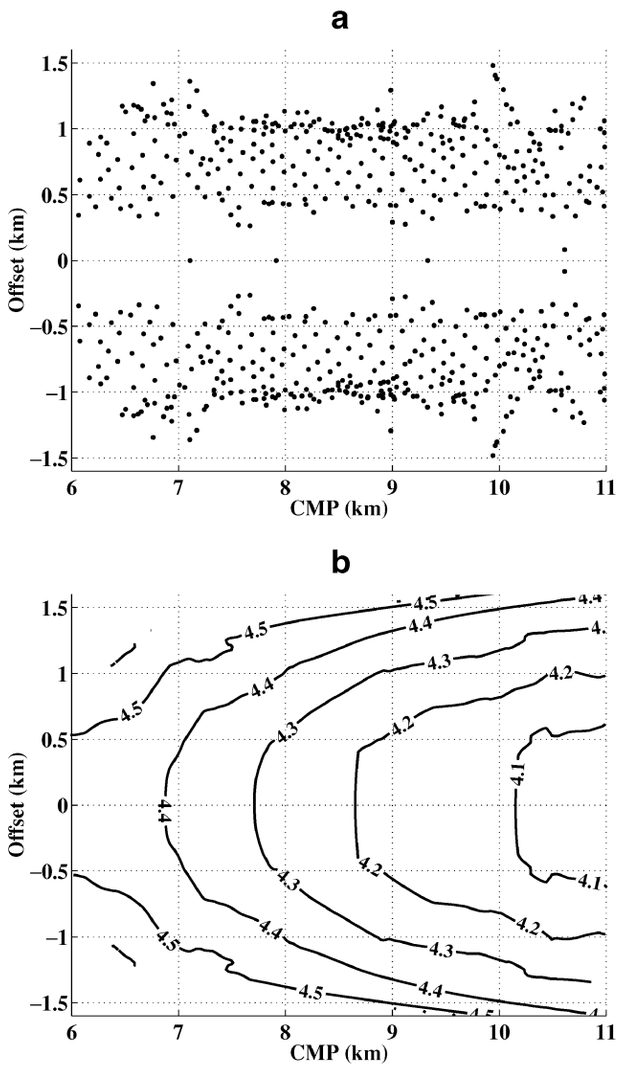

FIG. 4. (a) Computed positions of the shear-wave sources and receivers and (b) SS traveltimes (in seconds) for the top overpressure interface (see Figure 1).

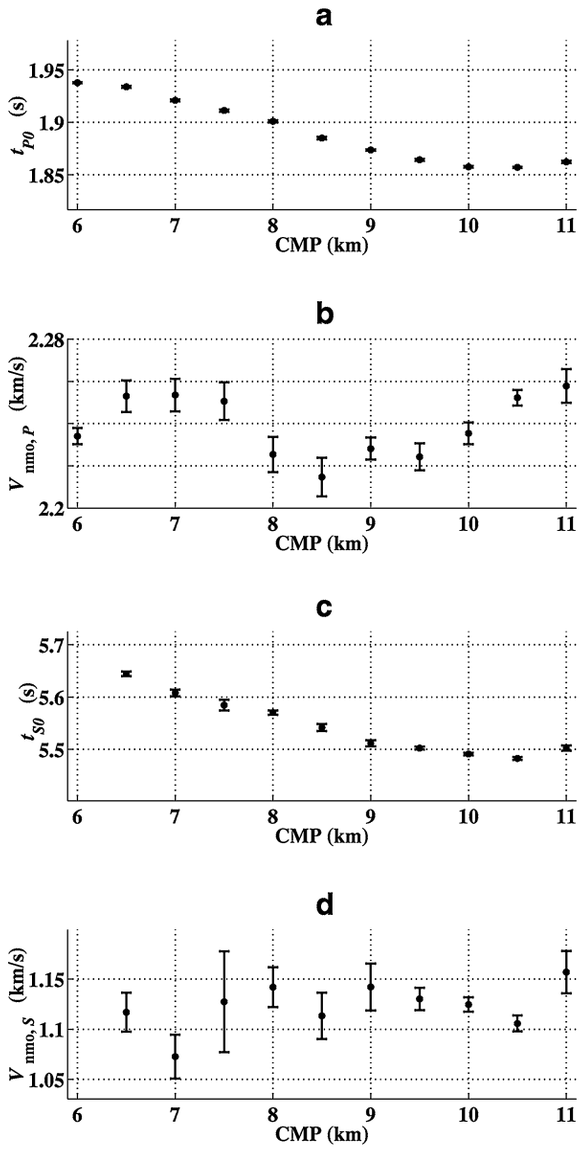

FIG. 5. Results of the velocity analysis for the top of the Balder formation: (a) $t_{P0}(x_{\mathrm{CMP}})$, (b) $V_{\mathrm{nmo},P}(x_{\mathrm{CMP}})$, (c) $t_{S0}(x_{\mathrm{CMP}})$, and (d) $V_{\mathrm{nmo},S}(x_{\mathrm{CMP}})$. The error bars correspond to the 95% confidence intervals.

traveltimes was carried out for all gathers containing ten or more source-receiver pairs. (Note the absence of results for $x_{\mathrm{CMP}} = 6$ km in Figures 5c and 5d.) The SS traveltimes are missing near the beginning of the line where the procedure of Grechka and Tsvankin (2002b) could not be performed because the needed PP and PS traveltime picks were not available (see Figures 2 and 4).

The error bars in Figure 5 were calculated assuming random (Gaussian) distribution of the traveltime picks around the best-fit hyperbolas. Although the data may be also distorted by systematic picking errors (for example, errors associated with incorrect identification of PP and PS events), those errors are difficult to evaluate or remove without additional information. The CMP gathers with errors significantly higher than those at adjacent locations (e.g., the shear-wave velocity pick at $x_{\mathrm{CMP}} = 7.5$ km in Figure 5d) were excluded from the anisotropic parameter estimation. In many cases, the larger error bars are associated with picking problems; the high level of noise in the input data may render the whole parameter-estimation procedure meaningless. Thus, only the most reliable portion of the data for CMP locations from 7–10 km was used for the parameter estimation.

Before describing the parameter-estimation results, we identify the properties of the estimated moveout velocities and traveltimes indicative of the presence of anisotropy. The zero-offset traveltimes t_{S0} and t_{P0} of the SS- and PP-waves for the top Balder (Figure 5) and other interfaces can be used to find the ratio of the vertical velocities V_{S0} and V_{P0} (assuming negligible dips):

$$g_0 \equiv \frac{V_{S0}}{V_{P0}} = \frac{t_{P0}}{t_{S0}}. \tag{7}$$

Also, velocity analysis yields the ratio of the corresponding NMO velocities $V_{\mathrm{nmo},S}$ and $V_{\mathrm{nmo},P}$:

$$g_{\mathrm{nmo}} \equiv \frac{V_{\mathrm{nmo},S}}{V_{\mathrm{nmo},P}}. \tag{8}$$

Note that all velocities represent effective (i.e., not interval) quantities estimated for a particular reflection event.

Figure 6 shows the ratios g_0 and g_{nmo} for the reflections from several interfaces marked in Figure 1. It is remarkable that for all examined events g_{nmo} (on average $\approx$0.45) is consistently and significantly greater than $g_0(\approx 0.3)$; note that g_{nmo} and g_0 are equal to each other in a homogeneous isotropic layer. In principle, the difference between g_{nmo} and g_0 can be caused by anisotropy, heterogeneity in isotropic media (Grechka and Tsvankin, 2003b), or a combination of these two factors. Appendix A shows, however, that even if the vertical variation of the interval S-wave velocity were orders of magnitude greater than that of the P-wave velocity, the obtained condition

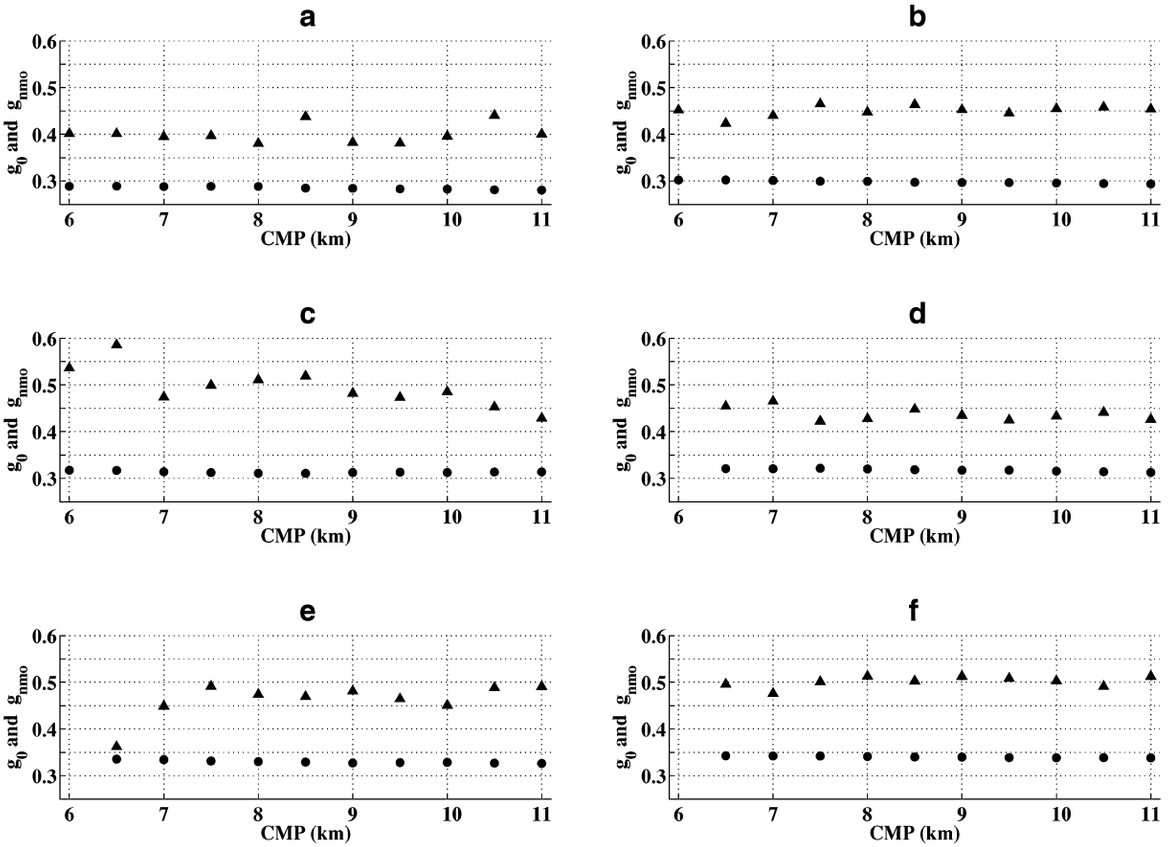

FIG. 6. The ratios g_0 (circles) and g_{nmo} (triangles) defined in equations (7) and (8) for the following horizons marked in Figure 1: (a) mid Miocene, (b) intra Oligocene, (c) base Oligocene, (d) top overpressure, (e) h8, and (f) top Balder.

$$\frac{g_0}{g_{\rm nmo}} \approx \frac{2}{3} \tag{9}$$

could be hardly satisfied in realistic vertically heterogeneous isotropic models. Therefore, we suggest that anisotropy is the only plausible explanation for the consistent deviation of $g_{\rm nmo}$ from g_0 in Figure 6.

Assuming that the interfaces are horizontal and the medium has VTI symmetry, we can find an approximate relationship between the anisotropic coefficients that explains the difference between the observed ratios $g_{\rm nmo}$ and g_0. For demonstration, let us treat the medium above each reflector in Figure 6 as a single homogeneous layer. Then, using the known expressions for the NMO velocities in VTI media (e.g., Tsvankin, 2001), equation (8) can be rewritten as

$$g_{\rm nmo} = \frac{V_{S0}\sqrt{1+2\sigma}}{V_{P0}\sqrt{1+2\delta}} = g_0\frac{\sqrt{1+2\sigma}}{\sqrt{1+2\delta}}, \tag{10}$$

where

$$\sigma \equiv \left(\frac{V_{P0}}{V_{S0}}\right)^2(\epsilon-\delta). \tag{11}$$

Substituting the estimates $g_{\rm nmo}=0.45$ and $g_0=0.3$ into equation (10) and dropping the quadratic terms in the anisotropic coefficients leads to the relationship

$$\epsilon \approx 0.06 + 1.25\delta. \tag{12}$$

Clearly, at least one of the anisotropic parameters cannot vanish, so matching of both PP and SS data requires the subsurface model to be effectively anisotropic. Below, we refine the crude estimate (12) of the effective ϵ and δ by performing a more elaborate inversion for the interval anisotropic coefficients.

ANISOTROPIC PARAMETER ESTIMATION

The most important issue to be addressed prior to the inversion is identification of the anisotropic parameters constrained by the available data. The low energy observed on the transverse displacement component (not shown here) suggests that either the medium is azimuthally isotropic (i.e., VTI or purely isotropic) or the line coincides with a vertical symmetry plane. Therefore, in the absence of wide-azimuth acquisition, it is natural to assume VTI symmetry in the inversion. Another indication that the VTI model is likely to be adequate is the predominantly horizontal layering above the reservoir, with dips less than 2°–3° (Figure 1).

Since the structure is almost horizontal and is assumed to be composed of VTI layers, PP and PS reflection data can be inverted for the NMO velocities and anellipticity parameter $\eta \equiv (\epsilon-\delta)/(1+2\delta)$, but not for the vertical velocities V_{P0} and V_{S0} and the coefficients ϵ and δ (Tsvankin and Grechka, 2000a; Grechka and Tsvankin, 2003a). In general, PP and PS reflection traveltimes in horizontally layered VTI media do not constrain reflector depth, even if the model parameters are selected in such a way that both PP and PS common-image gathers are flat and located at the same depth. Therefore, in the moveout-inversion procedure described below, the parameter δ is set to a certain predetermined value.

Inversion of reflection data for the interval VTI parameters

The input data include the PP traveltime picks and the computed SS traveltimes in the range $7 \le x_{\rm CMP} \le 10$ km from the mid Miocene, intra Oligocene, base Oligocene, h8, and top Balder horizons (see Figure 1). It is assumed that the model is composed of homogeneous VTI layers separated by planar interfaces of arbitrary dip.

First, we apply the tomographic algorithm of Grechka, Pech, and Tsvankin (2002) that operates with the zero-offset traveltimes, reflection slopes (i.e., ray parameters), and NMO velocities (in two dimensions) of PP- and SS-waves. For each trial set of the interval VTI parameters, we reconstruct the dips and depths of the interfaces using the zero-offset traveltimes and ray parameters, as described in Grechka, Pech and Tsvankin (2002). Then, the best-fit solution is found by minimizing the objective function

$$\mathcal{F}(\mathbf{m}) \equiv \sum_{Q,x_{\rm CMP},n}\left[V^{\rm calc}_{Q,{\rm nmo}}(x_{\rm CMP},n,\mathbf{m}) - V_{Q,{\rm nmo}}(x_{\rm CMP},n)\right]^2, \tag{13}$$

where $\mathbf{m}$ is the vector of unknown medium parameters that contains the interval vertical P- and S-wave velocities (V_{P0} and V_{S0}) and the anisotropic coefficients ϵ (the coefficient δ is fixed). Q denotes the mode (PP or SS), $n=1,2,\ldots,5$ is the reflector number, $V_{Q,{\rm nmo}}(x_{\rm CMP},n)$ are the measured PP- and SS-wave NMO velocities (such as those shown in Figures 5b and 5d), and $V^{\rm calc}_{Q,{\rm nmo}}(x_{\rm CMP},n,\mathbf{m})$ are the NMO velocities calculated for a given set of the model parameters $\mathbf{m}$.

Figure 7 displays the inversion results for five layers above the top Balder obtained for a fixed value of δ ($\delta=0$ in all layers). The error bars for the interval parameters, corresponding to 95% confidence intervals, were inferred from the errors in the zero-offset traveltimes and NMO (stacking) velocities (see Figure 5). Figure 8 shows inversion results similar to those in Figure 7, but this time obtained for a fixed $\delta=0.1$. Despite the substantial differences in all inverted parameters except for the reflector dips (found to be negligibly small), both models fit the data equally well. Indeed, the mean values of the least-squares objective function (13) for the two models differ by only 2%. Therefore, it is impossible to distinguish between these models using the combination of PP and PS traveltimes, which confirms the conclusions of Tsvankin and Grechka (2000a) and Grechka and Tsvankin (2003a).

With the reflector dips being so small (Figures 7e and 8e), we assume that all interfaces are horizontal and apply the conventional Dix formula to obtain the interval NMO velocities. Then, those velocities are combined with the ratios of the interval vertical P-wave and S-wave velocities to estimate the interval VTI parameters. After smoothing the effective NMO velocities, we performed this inversion for all CMP locations between 7 and 10 km; as before, the anisotropic parameter δ was fixed to ensure a unique result.

The coefficients ϵ of several equivalent anisotropic models obtained at four different CMP locations are plotted in Figure 9. All the models provide an excellent fit to the picked PP and PS traveltimes (the standard deviation of the computed traveltimes from the measured values does not exceed 0.3% for the top Balder reflection, see below). Although the estimated interval values of ϵ in each layer do change somewhat along the line, no statistically meaningful lateral variation

of ϵ is observed (the standard deviation of ϵ for a given δ is about 0.03).

Fitting of the original PP and PS traveltimes

The inversion results may be verified by comparing PP and PS moveouts computed for the equivalent anisotropic models with the input traveltime picks (such as those in Figure 2). Figure 10 displays typical ray-traced and measured (picked) PP and PS traveltimes for common midpoints between 7 and 10 km. In agreement with the above analysis of NMO velocities, the PP traveltimes for two distinctly different inverted VTI models fit the picks (dots) with high accuracy (Figures 10a and 10c). The average standard deviation of the computed PP traveltimes from the picked values for CMP locations 7 km $\le x_{\mathrm{CMP}} \le$ 10 km is only 6 ms, or about 0.3% of the average PP zero-offset traveltime. It is important to note that although the inversion was based on the zero-offset traveltimes and NMO velocities, the quality of fit in Figures 10a and 10c does not deteriorate at long offsets, reaching $1.7z$ (z is the reflector depth).

Figures 10b and 10d demonstrate that the inverted VTI models closely match the measured PS traveltimes as well. The standard deviation of the computed PS traveltimes from the corresponding picks is 12 ms, which is also 0.3% of the average converted-wave zero-offset traveltime. The absolute deviations for the PS-waves are larger than those for the PP-waves

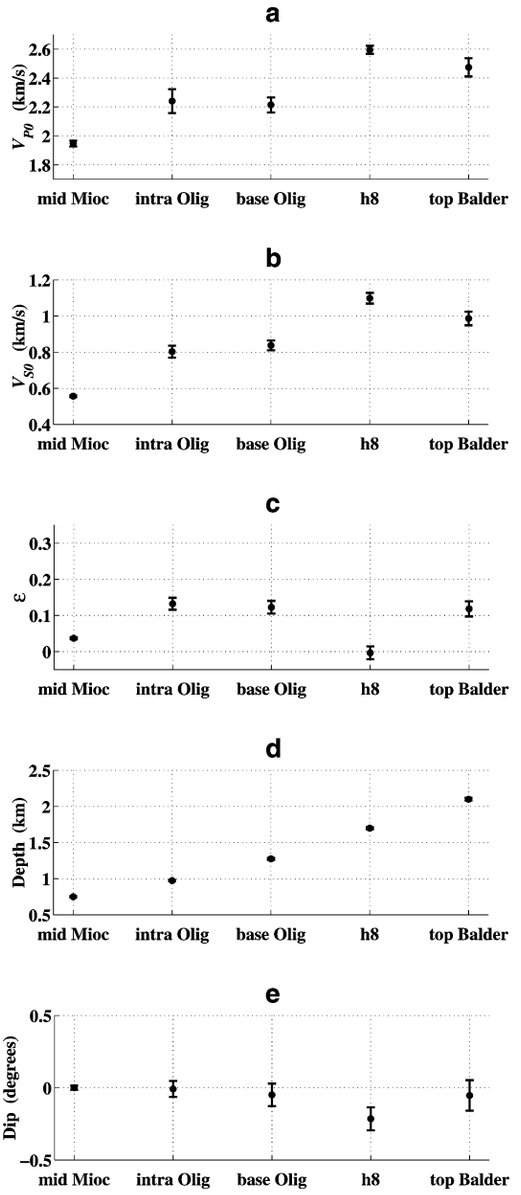

FIG. 7. Inverted interval VTI parameters V_{P0} (a), V_{S0} (b), and ϵ (c), and the reflector depths (d) and dips (e) for CMP locations 7 km $\le x_{\mathrm{CMP}} \le$ 10 km. The parameter $\delta = 0$ is fixed throughout the section.

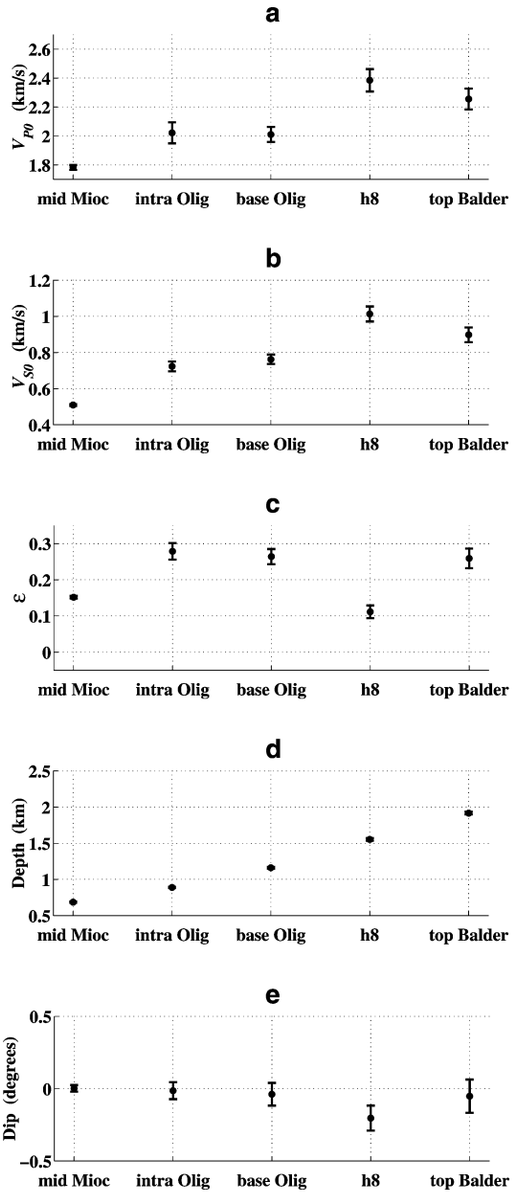

FIG. 8. Same as Figure 7, but for fixed $\delta = 0.1$.

because the PS data are noisier and have lower frequencies. Thus, we conclude that the family of VTI models obtained by our parameter-estimation procedure provides a good fit (given the level of noise) to the picked PP and PS traveltimes in the full range of available offsets.

The time section of PS-waves generated for this line using the laterally homogeneous VTI model from Figure 7 corresponding to $\delta = 0$ has a much higher quality than does the conventional isotropic section (Figure 11); similar results were obtained for other equivalent VTI models. In particular, the anisotropic processing substantially improved the image of the top of the reservoir and provided a crisp picture of faulting in the shallow part of the section. A more detailed discussion of the influence of anisotropy on converted-wave imaging and amplitude-variation-with-offset (AVO) analysis for this data set can be found in Grechka, Tsvankin, Bakulin, Hansen, and Signer (2002).

Constraining the inversion using check-shot data

The inherent nonuniqueness of the inversion of PP- and PS-wave reflection traveltimes in horizontally layered VTI media can be overcome if independent estimates of at least one model parameter (V_{P0}, V_{S0}, ϵ, δ, or reflector depth) are available. The most common source of such additional information is check shots or well logs obtained in boreholes. Here, we combine reflection data with P-wave traveltimes measured along well Siri-1 located close to $x_{\mathrm{CMP}} = 10$ km (data courtesy of Statoil).

Figure 12 shows the doubled vertical P-wave traveltimes t_{P0} (circles) recorded at five depth levels in well Siri-1. Since the smallest depth of the check shots corresponds approximately to the base of Oligocene, we had to extrapolate the traveltimes for the shallow part of the section and interpolate them between the measurements. The solid line in Figure 12 is the time-to-depth conversion curve used for the parameter estimation described below. The standard deviation of the check-shot data points from this curve is 5 ms, which is close to the standard deviation of the PP-wave reflection traveltime picks from the best-fit hyperbolas.

Once the reflector depths (the crosses in Figure 12) have been determined, the NMO velocities and zero-offset traveltimes of PP- and SS-waves can be inverted for the VTI parameters V_{P0}, V_{S0}, ϵ, and δ. The results displayed in Figure 13 were obtained by combining the interval NMO velocities (estimated using the Dix equation) and zero-offset traveltimes at CMP location $x_{\mathrm{CMP}} = 10$ km with the reflector depths from Figure 12. The standard deviations in the interval values of ϵ and δ do

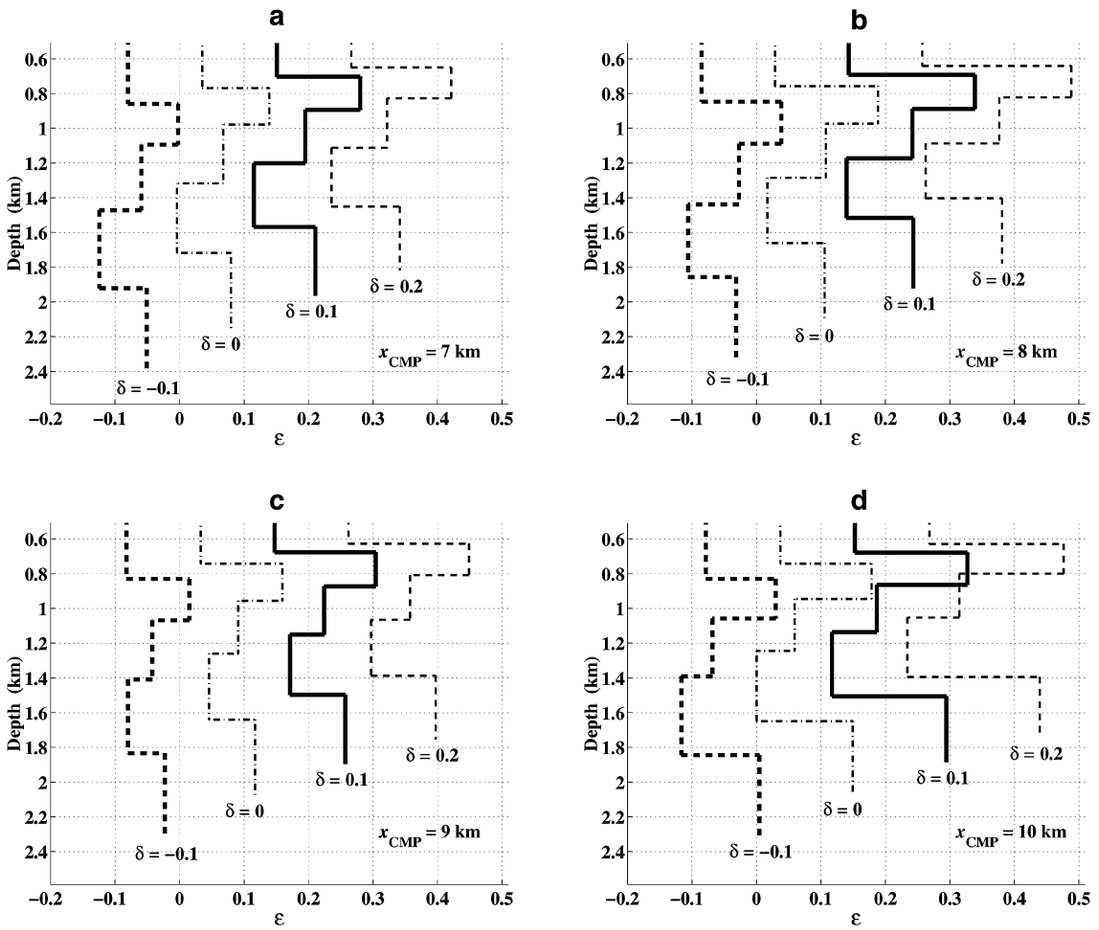

FIG. 9. Interval parameter ϵ estimated for CMP locations (a) 7 km, (b) 8 km, (c) 9 km, and (d) 10 km. The values of δ used to generate each ϵ curve are marked on the plots.

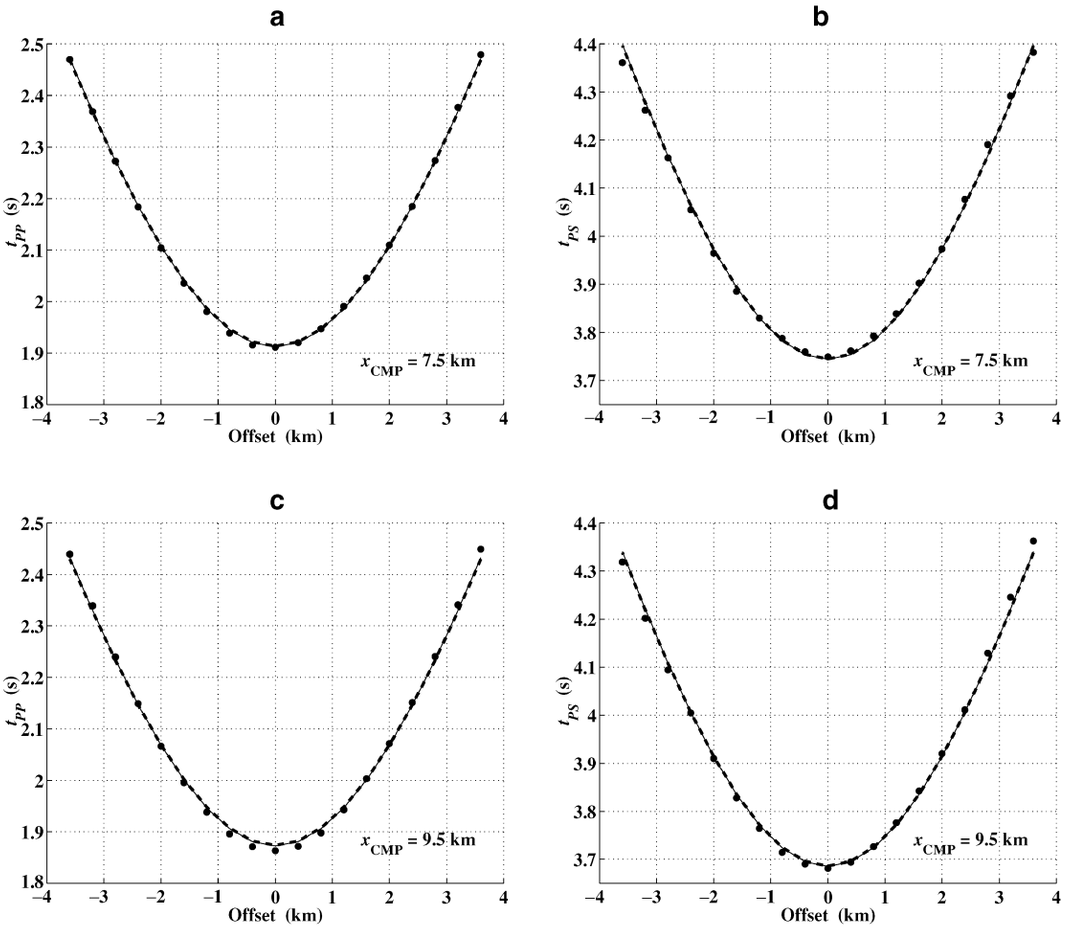

FIG. 10. Comparison of traveltimes picks (dots) with the modeled traveltimes for the reflections from the top of the Balder formation at two CMP locations (7.5 and 9.5 km): (a) and (c) are PP traveltimes, (b) and (d) are PS traveltimes. The solid and dashed lines correspond to the traveltimes computed for the inverted models marked by the dots in Figures 7 ($\delta = 0$) and 8 ($\delta = 0.1$), respectively.

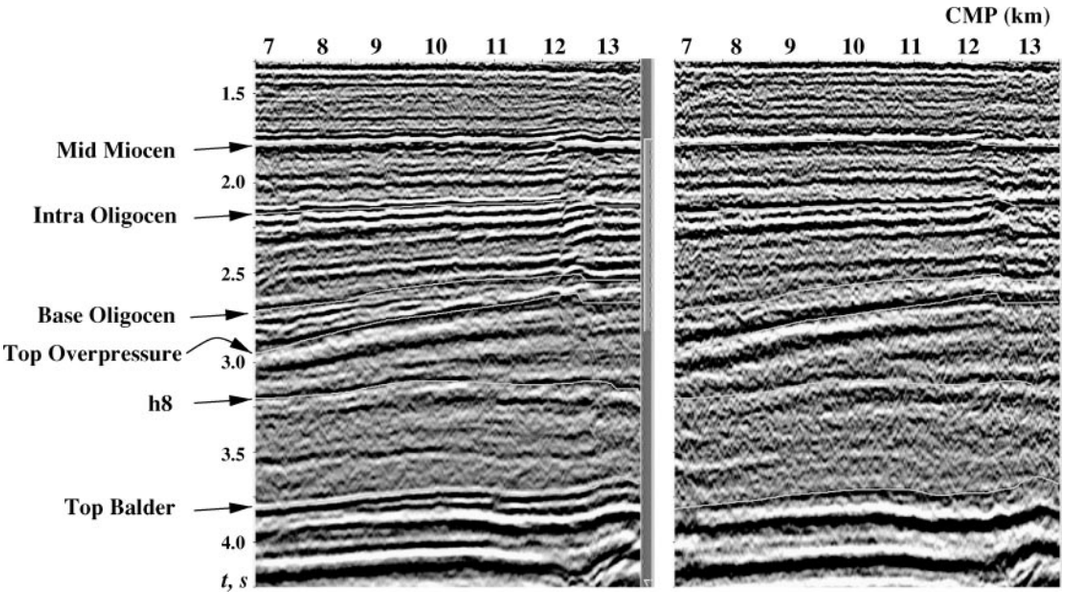

FIG. 11. Common-conversion point stacks for the VTI model with $\delta = 0$ (left) and the isotropic model with $\epsilon = \delta = 0$ (right).

not exceed 0.03. Clearly, δ varies with depth, which violates the artificial assumption of constant δ used in the inversion above.

The largest interval values of ϵ and δ are observed in the middle part of the section, with ϵ reaching almost 0.25 in the Oligocene layer. Although δ becomes small in the layer immediately above the reservoir, the values of $\epsilon \approx 0.17$ indicate that anisotropy in this layer is quite significant for both P-waves and, particularly, PS-waves (the corresponding interval σ is about 0.5). Also, note that throughout the section $\epsilon > \delta$, which means that the parameters η and σ are positive. This result is consistent with the predominantly positive values of η obtained in other case studies for VTI media (e.g., Alkhalifah et al., 1996; Tsvankin, 2001).

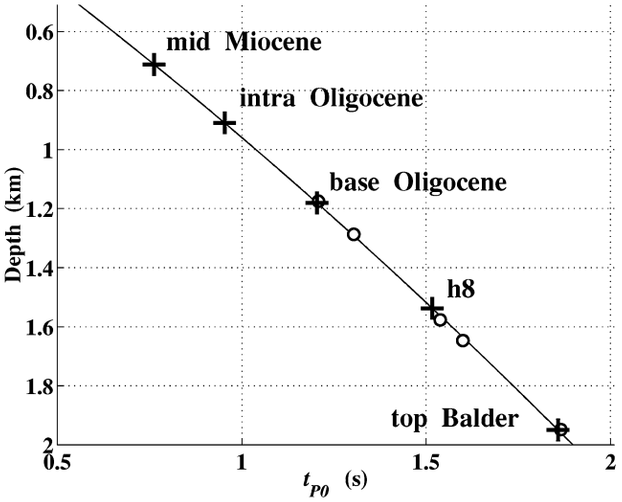

FIG. 12. P-wave check-shot data (circles) acquired in well Siri-1; the traveltimes were doubled for comparison with reflection data. The solid line marks the interpolated and extrapolated traveltime; the crosses correspond to the zero-offset reflection traveltimes t_{P0} for several horizons at common midpoint $x_{\mathrm{CMP}} = 10$ km.

Since the interval vertical velocities V_{P0} and V_{S0} and the anisotropic coefficients ϵ and δ describe the VTI model (for P- and SV-waves) at the well location, they cannot be extrapolated along the line without using additional borehole data or making some assumptions about the lateral variation of the medium parameters. For example, the absence of statistically meaningful variations of $\epsilon(x_{\mathrm{CMP}})$ (Figure 9) suggests that its interval values shown in Figure 13b can be used to estimate the parameters $V_{P0}(x_{\mathrm{CMP}})$, $V_{S0}(x_{\mathrm{CMP}})$, and $\delta(x_{\mathrm{CMP}})$ for the whole range of CMP locations. Since the dips in this section are so small, another possible assumption is to fix the reflector depths at the values shown in Figure 12 (i.e., make the reflectors horizontal) and estimate the vertical velocities and anisotropic coefficients along the line. Neither of these assumptions, however, can be fully verified based on the available data.

DISCUSSION

Accounting for subsurface anisotropy might require changing some model-building approaches adopted by the oil industry. The results of this study allow us to speculate about possible ways of using multicomponent surveys for constructing an accurate anisotropic depth model. Whereas P-wave imaging is prone to significant depth uncertainty in the presence of anisotropy, combining PP and PS data might help to estimate the vertical velocities and reflector depths. If the subsurface contains dipping structures, anisotropy leads to both depth and lateral mispositioning of reflecting horizons. Tsvankin and Grechka (2000a, b) showed that if reflector dips in VTI media exceed 15°, traveltimes of the PP- and PS-waves can be inverted for all relevant parameters including the vertical P- and S-wave velocities. Imaging with the estimated VTI velocity field can provide accurate spatial locations of the exploration targets.

For models composed of nearly horizontal VTI layers, as in the case of the Siri reservoir, surface PP and PS data cannot be uniquely inverted for the vertical velocities and Thomsen parameters. Still, the methodology described here is more general and flexible than approaches that artificially select a particular VTI model by assuming a priori that $\delta = 0$ (Nolte et al., 1999; Sayers and Johns, 1999). Knowledge of regional

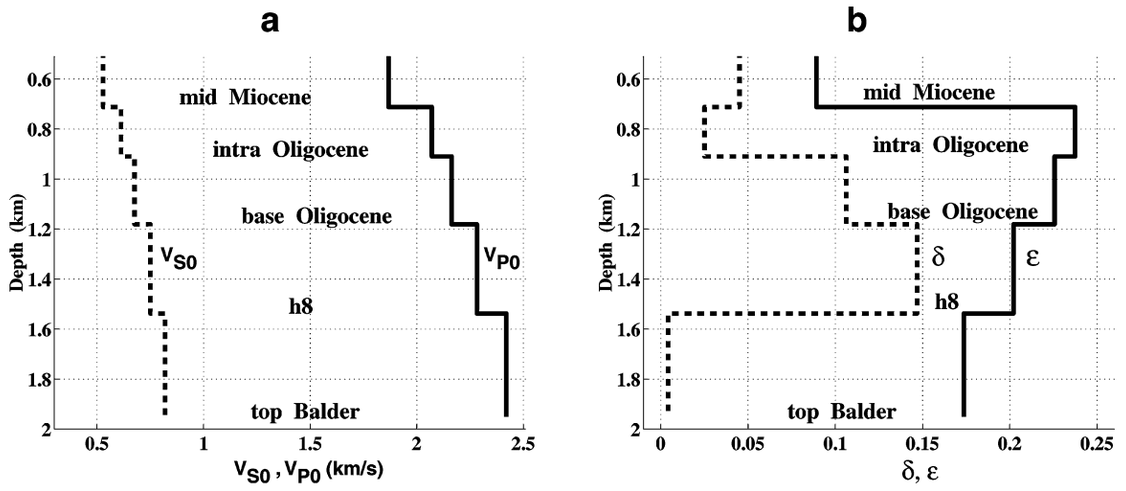

FIG. 13. Inversion of the reflection and check-shot (see Figure 12) data at CMP location $x_{\mathrm{CMP}} = 10$ km: (a) interval vertical velocities V_{S0} (dashed) and V_{P0} (solid); (b) interval anisotropic coefficients δ (dashed) and ϵ (solid).

lithology can help to constrain at least one of the medium parameters (e.g., the parameter δ or one of the vertical velocities), which is sufficient to eliminate the ambiguity in the inversion of reflection data. Alternatively, while drilling of the first well in a certain field is in progress, logging-while-drilling (seismic-while-drilling) may provide the P- and S-wave velocities and reflector depths along the borehole. This information can be used in the inversion of surface data to estimate the anisotropic coefficients in the upper part of the section and to obtain a more accurate solution for the deeper horizons (i.e., updating the model in real time). After the well has been drilled, it is possible to construct a VTI depth model consistent with both surface seismic and borehole data.

The anisotropic subsurface model determined from multicomponent data has a wide range of applications, from depth imaging to reservoir characterization and monitoring. To predict such reservoir properties as pore pressure and fluid saturation, it is common to employ empirical relationships for the P- and S-wave velocities. In the presence of anisotropy, however, those techniques are difficult to implement because the velocity at each spatial location is directionally dependent. For example, most existing AVO algorithms operate on (incidence) angle gathers rather than in the offset domain (Castagna and Backus, 1993). Therefore, if the overburden is anisotropic, even the first step of AVO analysis (mapping the data from offsets to the corresponding incidence angles) requires accounting for anisotropy above the target horizon. Distortions in the conventional AVO inversion are also caused by amplitude focusing phenomena in the anisotropic overburden and by the anisotropic terms in the reflection coefficient (Tsvankin, 1995, 2001). The influence of anisotropy above the Siri reservoir on AVO analysis and imaging is discussed by Grechka, Tsvankin, Bakulin, Hansen, and Signer (2002).

Therefore, the methodology used here can be instrumental in improving the results of AVO analysis and other reservoir-characterization methods by providing an accurate spatially varying anisotropic velocity field. Also, the estimated anisotropic parameters are closely related to the petrophysical parameters and stress conditions of the reservoir.

CONCLUSIONS

1) This study confirms the feasibility of obtaining accurate prestack traveltime picks on 2-D multicomponent field data. Despite the presence of picking errors, the quality of the picked traveltimes was sufficient for velocity analysis and anisotropic model-building.
2) The 2-D version of the methodology of Grechka and Tsvankin (2002b) for constructing pure SS-wave reflection traveltimes from PP and PS data was successfully tested on field data. It should be emphasized that this procedure does not require knowledge of the velocity field.
3) The parameters of the assumed VTI model were determined from joint stacking-velocity tomography of PP- and SS-waves (Grechka, Pech, and Tsvankin, 2002). A relatively low computational cost and the possibility of gaining analytic insight into the constrained parameter combinations are the major advantages of stacking-velocity tomography over more conventional tomographic algorithms, which operate directly with traveltimes. In particular, restricting the input data to stacking (moveout) velocities increases the computational speed of the forward-modeling part of the tomographic algorithm by several orders of magnitude.
4) Since the model was close to horizontally layered, the combination of PP and PS reflection traveltimes could not constrain the four relevant interval VTI parameters: the P- and S-wave vertical velocities V_{P0} and V_{S0}, and the anisotropic coefficients ϵ and δ. Therefore, instead of trying to find a single "best-fit" solution, we obtained a number of equivalent anisotropic models that fit reflection traveltimes equally well and produce high-quality time images of the subsurface.
5) Independent information about the reflector depths obtained from borehole data (i.e., P-wave check shots) was used to remove the ambiguity in parameter estimation and build a VTI model suitable for depth imaging.

ACKNOWLEDGMENTS

We are grateful to members of the A(nisotropy)-Team of the Center for Wave Phenomena (CWP), Colorado School of Mines (CSM), for helpful discussions. We thank Schlumberger for permission to publish this case study, WesternGeco for providing the reflection data, and Statoil for releasing the check shots. Reviews by Ken Larner (CSM), Ralf Ferber and Dave Nichols (both of Schlumberger) helped to improve the manuscript. The paper also benefited from the constructive suggestions of the associate editor and the reviewers of GEOPHYSICS. The support for Vladimir Grechka and Ilya Tsvankin was provided by the members of the Consortium Project on Seismic Inverse Methods for Complex Structures at CWP and by the Chemical Sciences, Geosciences and Biosciences Division, Office of Basic Energy Sciences, U.S. Department of Energy.

REFERENCES

Alkhalifah, T., Tsvankin, I., Larner, K., and Toldi, J., 1996, Velocity analysis and imaging in transversely isotropic media: Methodology and a case study: The Leading Edge, **15**, 371–378.

Ayres, A., and Theilen, F., 1999, Relationship between P- and S-wave velocities and geological properties of near-surface sediments of the continental slope of the Barents Sea: Geophys. Prosp., **47**, 431–441.

Bakulin, A., Grechka, V., and Tsvankin, I., 2000, Estimation of fracture parameters from reflection seismic data—Part I: HTI model due to a single fracture set: Geophysics, **65**, 1788–1802.

Castagna, J. P., and Backus, M., Eds, 1993, Offset dependent reflectivity—Theory and practice of AVO analysis: Soc. Expl. Geophys.

Dix, C. H., 1955, Seismic velocities from surface measurements: Geophysics, **20**, 68–86.

Grechka, V., Pech, A., and Tsvankin, I., 2000a, Inversion of P-wave data in laterally heterogeneous VTI media. Part I: Plane dipping interfaces: 70th Ann. Internat. Mtg., Soc. Expl. Geophys., Expanded Abstracts, 2225–2228.

——— 2000b, Inversion of P-wave data in laterally heterogeneous VTI media. Part II: Irregular interfaces: 70th Ann. Internat. Mtg., Soc. Expl. Geophys., Expanded Abstracts, 2229–2232.

——— 2002, Multicomponent stacking-velocity tomography for transversely isotropic media: Geophysics, **67**, 1564–1574, this issue.

Grechka, V., and Tsvankin, I., 2002a, NMO-velocity surfaces and Dix-type formulas in anisotropic heterogeneous media: Geophysics, **67**, 939–951.

——— 2002b, $PP+PS=SS$: Geophysics, in press.

——— 2003a, On the joint nonhyperbolic moveout inversion of PP and PS data in VTI media: Geophysics, in press.

——— 2003b, Processing-induced anisotropy: Geophysics, in press.

Grechka, V., Tsvankin, I., Bakulin, A., Hansen, J. O., and Signer, C., 2002, Anisotropic inversion and imaging of PP and PS reflection data in the North Sea: The Leading Edge, **21**, 90–97.

Iversen, E., and Gjøystdal, H., 1996, Event-oriented velocity estimation based on prestack data in time or depth domain: Geophys. Prosp., **44**, 643–686.
Iversen, E., Gjøystdal, H., and Hansen, J. O., 2000, Prestack map migration as an engine for parameter estimation in TI media: 70th Ann. Internat. Mtg., Soc. Expl. Geophys., Expanded Abstracts, 1004–1007.
Muyzert, E., 2000, Scholte wave velocity inversion for a near surface S-velocity model and PS-statics: 70th Ann. Internat. Mtg., Soc. Expl. Geophys., Expanded Abstracts, 1197–1200.
Nolte, B., Bishop, K., and Sukup, D., 1999, Anisotropic prestack depth migration of converted-wave data from the Gulf of Mexico: 69th Ann. Internat. Mtg., Soc. Expl. Geophys., Expanded Abstracts, 691–694.
Sayers, C., and Johns, T., 1999, Anisotropic velocity analysis using marine 4-C seismic data: 69th Ann. Internat. Mtg., Soc. Expl. Geophys., Expanded Abstracts, 780–783.
Signer, C., Hansen, J. O., Hutton, G., Nickel, M., Reymond, B., Schlaf, J., Sønneland, L., Tjøstheim, B., and Veire, H. H., 2000, Reservoir characterization using 4C seismic and calibrated 3D AVO: *in* Ofstad, K., Kittilsen, J. E., and Alexander-Marrack, P., Eds., Improving the exploration process by learning from the past: Elsevier Science Publ. Co., Inc.
Tessmer, G., and Behle, A., 1988, Common reflection point data-stacking technique for converted waves: Geophys. Prosp., **36**, 671–688.
Thomsen, L., 1986, Weak elastic anisotropy: Geophysics, **51**, 1954–1966.
——— 1999, Converted-wave reflection seismology over inhomogeneous, anisotropic media: Geophysics, **64**, 678–690.
Tsvankin, I., 1995, Body-wave radiation patterns and AVO in transversely isotropic media: Geophysics, **60**, 1409–1425.
——— 2001, Seismic signatures and analysis of reflection data in anisotropic media: Elsevier Science Publ. Co., Inc.
Tsvankin, I., and Grechka, V., 2000a, Dip moveout of converted waves and parameter estimation in transversely isotropic media: Geophys. Prosp., **48**, 257–292.
——— 2000b, Two approaches to anisotropic velocity analysis of converted waves: 70th Ann. Internat. Mtg., Soc. Expl. Geophys., Expanded Abstracts, 1193–1196.

APPENDIX A

INFLUENCE OF LAYERING ON THE VERTICAL AND STACKING VELOCITIES

Suppose the overburden above the Siri reservoir is isotropic and vertically heterogeneous. The goal of this appendix is to show that realistic vertical velocity variations cannot produce the observed discrepancy between the ratios g_0 and $g_{\rm nmo}$ (Figure 6):

$$\frac{g_0}{g_{\rm nmo}} = \frac{V_{S0}}{V_{{\rm nmo},S}} \frac{V_{{\rm nmo},P}}{V_{P0}} \approx \frac{2}{3}. \tag{A-1}$$

The effective vertical velocity V_{Q0} ($Q = P$ or $Q = S$) is defined as the ratio of the reflector depth z to the one-way zero-offset traveltime τ_{Q0}:

$$V_{Q0} = \frac{z}{\tau_{Q0}} = \frac{\sum\limits_n \Delta z_n}{\sum\limits_n \Delta z_n / V_{Q0,n}}, \tag{A-2}$$

where Δz_n are the layer thicknesses, $V_{Q0,n}$ are the interval velocities, and n is the layer number. In contrast, the effective stacking (NMO) velocity is determined from a different type of interval-velocity averaging specified by the Dix (1955) formula:

$$V^2_{{\rm nmo},Q} = V_{Q0} \frac{\sum\limits_n \Delta z_n V_{Q0,n}}{\sum\limits_n \Delta z_n}. \tag{A-3}$$

Hence, the ratio of the effective NMO and vertical velocities is given by

$$\frac{V_{{\rm nmo},Q}}{V_{Q0}} = \left\{ \left[\frac{\sum\limits_n \Delta z_n V_{Q0,n}}{\sum\limits_n \Delta z_n} \right] \left[\frac{\sum\limits_n \Delta z_n / V_{Q0,n}}{\sum\limits_n \Delta z_n} \right] \right\}^{1/2}. \tag{A-4}$$

According to the Cauchy-Schwartz inequality, the ratio $V_{{\rm nmo},Q}/V_{Q0}$ is always greater than or equal to unity (Grechka and Tsvankin, 2003b). In the special case of constant Δz_n, $V_{{\rm nmo},Q}/V_{Q0}$ reduces to the square-root of the ratio of the arithmetic and harmonic averages of the interval velocities $V_{Q0,n}$; it is well known that this ratio cannot be smaller than unity.

Therefore, the effective velocities in equation (A-1) satisfy the inequalities

$$\frac{V_{S0}}{V_{{\rm nmo},S}} \le 1 \quad \text{and} \quad \frac{V_{{\rm nmo},P}}{V_{P0}} \ge 1. \tag{A-5}$$

Clearly, in the presence of vertical heterogeneity alone, the terms $V_{S0}/V_{{\rm nmo},S}$ and $V_{{\rm nmo},P}/V_{P0}$ in equation (A-1) tend to compensate each other, and the ratio $g_0/g_{\rm nmo}$ is expected to be relatively close to unity. Below, we examine several interval vertical-velocity functions $V_{P0}(z)$ and $V_{S0}(z)$ and show that the ratio $g_0/g_{\rm nmo} \approx 2/3$ in equation (A-1) should be considered as highly anomalous for realistic isotropic models.

Example 1: Constant gradients of V_{P0} and V_{S0}

We begin with the simplest type of vertically heterogeneous isotropic media in which both interval velocities $V_{P0}(z)$ and $V_{S0}(z)$ are linear functions of the depth z (Figure A-1a). The

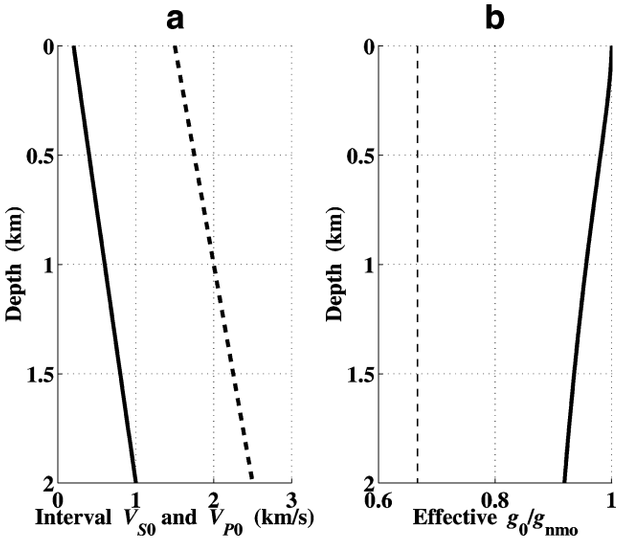

FIG. A-1. (a) Linear interval velocity functions $V_{P0}(z) = 1.5 + 0.5z$ (dashed line) and $V_{S0}(z) = 0.2 + 0.4z$ (solid line); (b) the corresponding ratio $g_0/g_{\rm nmo}$ (solid line) and the value $g_0/g_{\rm nmo} = 2/3$ (dashed line).

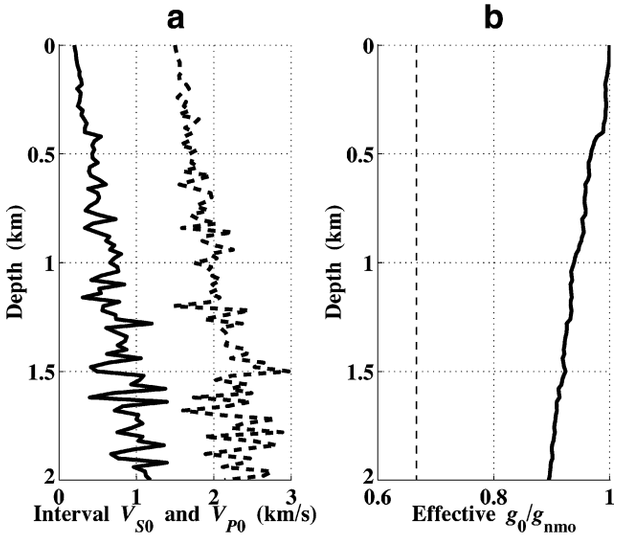

FIG. A-2. Same as Figure A-1, but with depth-dependent random variations added to the interval velocities $V_{P0}(z) = 1.5 + 0.5z$ and $V_{S0}(z) = 0.2 + 0.4z$.

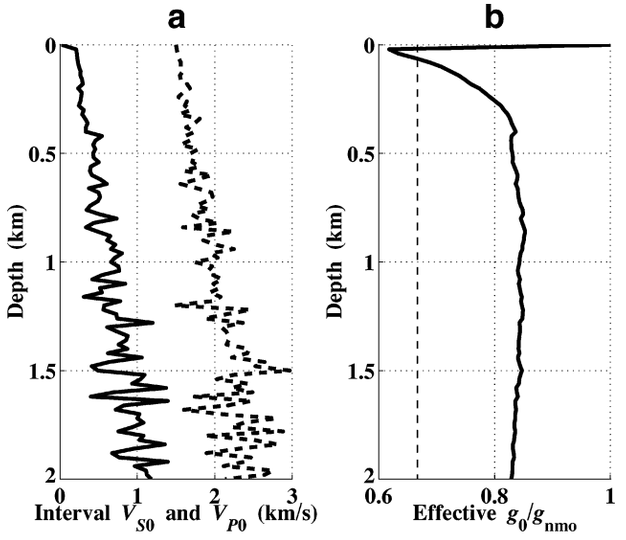

FIG. A-3. Same as Figure A-2, but the S-wave velocity model contains a layer with an extremely low S-wave interval velocity $V_{S0}(z) = 25$ m/s for $0 \le z \le 20$ m.

P-wave velocity at the ocean bottom (i.e., at zero depth) is $V_{P0}(0) = V_w = 1.5$ km/s, whereas the chosen value for S-waves $V_{S0}(0) = 0.2$ km/s was obtained by Muyzert (2000) for underwater sediments. The vertical gradients for P- and S-wave velocities are selected in such a way that $V_{P0}(z)$ and $V_{S0}(z)$ at the depth $z = 2$ km are close to the interval velocities for the horizon immediately above the top of the Balder formation (Figure 7).

Figure A-1a shows that for the depth range from $z = 0$ to $z = 2$ km, the S-wave interval velocity V_{S0} increases by a factor of 5 compared to a factor of 1.7 for the P-wave velocity. Although the vertical heterogeneity for S-waves is much greater than that for P-waves, it still cannot make the ratio $g_0/g_{\rm nmo}$ smaller than 0.92 (Figure A-1b). Therefore, vertical velocity gradient is clearly insufficient to reduce the ratio $g_0/g_{\rm nmo}$ to values close to 2/3.

Example 2: Random variations of V_{P0} and V_{S0}

To make the interval velocity variations more realistic, we add a random component to the linear velocity functions (Figure A-2a). The random variations, however, have a relatively minor influence on the ratio $g_0/g_{\rm nmo}$ (compare Figures A-2b and A-1b). Thus, high-frequency components of the interval P- and S-wave velocities cannot explain the observed low values of $g_0/g_{\rm nmo}$.

Example 3: Extremely low underwater S-wave velocity

The ratio $g_0/g_{\rm nmo}$ can be reduced by increasing the magnitude of the shear-wave velocity heterogeneity. For example, it is possible for the velocity V_{S0} near the ocean bottom to be as small as 25 m/s (Figure A-3a). Such uncommonly low velocities were reported by Ayres and Theilen (1999) in unconsolidated ocean-bottom sediments. Although the ratio $g_0/g_{\rm nmo}$ does drop below 2/3 at small depths, it quickly increases with depth to values exceeding 0.8 as the influence of the rapid velocity variation in the shallow part of the section becomes less pronounced (Figure A-3b). Therefore, we conclude that it is hardly possible to find a realistic vertically heterogeneous isotropic model for which the ratio $g_0/g_{\rm nmo}$ stays as small as 2/3 over a wide depth range.